SIAM J. SCI. COMPUT.
Vol. 43, No. 3, pp. A1997–A2018

A CONTINUOUS PERSPECTIVE ON SHAPE OPTIMIZATION VIA DOMAIN TRANSFORMATIONS*

J. HAUBNER†, M. SIEBENBORN‡, AND M. ULBRICH†

Abstract. In this article we consider shape optimization problems as optimal control problems via the method of mappings. Instead of optimizing over a set of admissible shapes, a reference domain is introduced, and it is optimized over a set of admissible transformations. The focus is on the choice of the set of transformations, which we motivate from a continuous perspective. In order to guarantee local injectivity of the admissible transformations, we enrich the optimization problem by a nonlinear constraint. Numerical results for drag minimization of Stokes flow are presented.

Key words. shape optimization, method of mappings, Stokes flow

AMS subject classifications. 35R30, 49K20, 49Q10, 65K10

DOI. 10.1137/20M1332050

1. Introduction.

Shape optimal design is a vivid research field with a wide range of applications, including fluid dynamics [33, 3, 12], acoustics [42], magnetostatics [11], image restoration and segmentation [17], interface identification in transmission processes [35, 14, 30], nano-optics [18], and composite material identification [37, 30].

In shape optimization, a shape functional $\tilde{j} : \mathcal{O}_{\text{ad}} \to \mathbb{R}$ is optimized over a set of admissible shapes $\mathcal{O}_{\text{ad}}$, i.e.,

$$\min_{\Omega \in \mathcal{O}_{\text{ad}}} \tilde{j}(\Omega). \tag{1.1}$$

There are various ways to tackle this problem. In this work, we focus on the method of mappings [29, 3, 22, 10, 15]. Here, the optimization problem (1.1) is reformulated as an optimization problem over a set of admissible transformations $\mathcal{T}_{\text{ad}}$ defined on a nominal domain Ω,

$$\min_{\tau \in \mathcal{T}_{\text{ad}}} j(\tau), \tag{1.2}$$

where $j(\tau) \coloneqq \tilde{j}(\tau(\Omega))$, which allows to consider shape optimization problems in the optimal control framework.

Mesh degeneration of a finite element denotes a significant increase of the ratio of largest inscribed to smallest circumscribed sphere radius. It is one of the bottlenecks

*Submitted to the journal's Methods and Algorithms for Scientific Computing section April 15, 2020; accepted for publication (in revised form) January 11, 2021; published electronically June 3, 2021.

https://doi.org/10.1137/20M1332050

Funding: The first and third authors received support from the Deutsche Forschungsgemeinschaft (German Research Foundation) as part of the International Research Training Group IGDK 1754 "Optimization and Numerical Analysis for Partial Differential Equations with NonSmooth Structures," project number 188264188/GRK1754. The second author acknowledges the support by the Deutsche Forschungsgemeinschaft within the Research Training Group GRK 2583 "Modeling, Simulation and Optimization of Fluid Dynamic Applications."

†Department of Mathematics, Technical University of Munich, Boltzmannstr. 3, 85748 Garching bei München, Germany (haubnerj@ma.tum.de, mulbrich@ma.tum.de).

‡Department of Mathematics, University of Hamburg, Bundesstr. 55, 20146 Hamburg, Germany (martin.siebenborn@uni-hamburg.de).

in performing transformation-based shape optimization techniques; see, e.g., [9]. On the one hand, by the modeling of the optimization problem, it has to be ensured that the boundary of the transformed domain is not self-intersecting. This can, e.g., be realized using bounds on the deformation in combination with geometrical constraints, such as volume and barycenter constraints. On the other hand, mesh degeneration might also appear for large deformations even if the boundary of the domain is not self-intersecting. Therefore, finding transformations that preserve the mesh quality is an active field of research. In [20] it is proposed to work with an extension of the boundary deformation that preserves the mesh quality. This method, however, is limited to 2d cases. Another approach is remeshing; see, e.g., [45, 8, 2]. Compared to directly applying a displacement w, the quality of the mesh can be improved by using a transformation $\tau(\Omega) = (\mathrm{id} + \psi(w))(\Omega)$ such that $\tau(\Omega) = (\mathrm{id} + w)(\Omega)$, where $\psi(w)$ is either defined via the solution of a partial differential equation (PDE) or via a solution of an optimization problem. These methods allow for node relocations without changing the deformed domain. Other approaches project the shape gradient to mimic the continuous behavior motivated through the Hadamard–Zolésio structure theorem [9] or work with extension equations that require parameter tuning in order to avoid mesh degeneration [34, 36, 11]. However, finding adequate parameters for a given extension equation tends to be a time-consuming effort. Moreover, the empirically determined parameters are typically tailored for one specific mesh and problem setting.

We consider the problem from a continuous perspective and require sufficiently high regularity of the boundary deformations analogous to [25, 38, 24, 3], where parametrizations of the design boundary with sufficiently high regularity are used. Our approach ensures that all admissible controls yield transformations that map the reference domain Ω to Lipschitz (or even smoother) domains, which is needed for the existence and regularity theory of the PDEs that appear as constraints in the shape optimization problem. Since the optimization problem is formulated in the continuous setting, this approach also allows for refinement and remeshing techniques. In contrast, if one considers the problem only from a discretized point of view, remeshing also requires a reinitialization of the optimization algorithm. However, an accurate modeling remains challenging since, on the one hand, the most general setting, i.e., working with transformations in $W^{1,\infty}(\Omega)^d$, is difficult since it is a nonreflexive Banach space. On the other hand, working with smoother spaces often requires H^2-conforming finite element methods as used in [24].

In this work, we focus on the modeling of the shape optimization problem respecting the continuous requirements on the transformations. On the one hand, for the optimization, it is convenient to work in a Hilbert space setting since, e.g., gradients can be determined via the Riesz representation theorem. On the other hand, one ideally wants to work with a set of admissible transformations that only contains bi-Lipschitz transformations but allows for functions that are less regular than $\mathcal{C}^1$ in order to enable the forming of kinks in the design boundary. The standard H^s-spaces do not fulfill this requirement. As a remedy, we work with (too) regular transformations and consider a sequence of decreasing regularization parameters to approximate the kink with a sequence of smooth domains. Motivated by the theoretical considerations in section 2, we work in Banach spaces X, Y such that $Y \hookrightarrow \mathcal{C}^1(\overline{\Omega})^d$ and with a continuous mapping $S : X \to Y$. In addition, we enrich the optimization problem

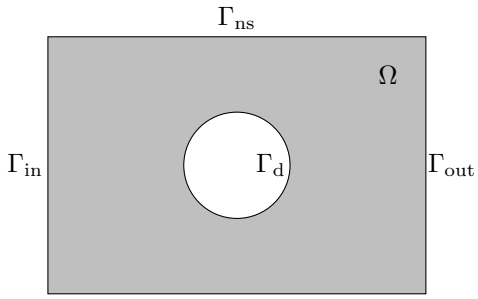

FIG. 1.1. *2d sketch of the geometrical configuration for a shape optimization problem that is governed by Stokes flow.*

with additional constraints and investigate

$$
\begin{aligned}
&\min_{c\in X} j(\tau) + \frac{\alpha}{2}\|c\|_X^2 \\
&\text{s.t. } \tau = \mathrm{id} + w, \\
&\qquad g(w) = 0, \\
&\qquad w = S(c), \\
&\qquad \|c\|_X \le \eta_2, \\
&\qquad \det(D(\mathrm{id}+w)) \ge \eta_1 \quad \text{in } \Omega
\end{aligned}
\tag{1.3}
$$

for $\eta_1 \in (0,1)$ and $\eta_2 > 0$, where g represents geometric constraints, e.g., volume and barycenter constraints, and c denotes a scalar-valued function on the design part Γ_{d} of the boundary of Ω. We choose S such that the regularity requirements are fulfilled in two and three dimensions and work on Hilbert spaces. Therefore, we require $Y \hookrightarrow H^{\frac{5}{2}+\epsilon}(\Omega)$ with $\epsilon > 0$. To circumvent the use of H^2-conforming finite elements due to computational performance aspects, the regularity is lifted stepwise, which is inspired by mixed finite element methods; see, for instance, [5]. In this paper, we focus on an approach that starts with a design parameter $c \in L^2(\Gamma_{\text{d}})$ that is mapped to a function $b \in H^2(\Gamma_{\text{d}})$ by solving a Laplace–Beltrami equation. Imposing b as Neumann boundary condition for an elliptic extension equation, we obtain a deformation field w. However, there are various other possibilities. Alternatively, one could also start with $c \in H^1(\Gamma_{\text{d}})$ and impose b as Dirichlet boundary condition for the elliptic extension equation. Compared to previous approaches, the only difference is the additional Laplace–Beltrami equation, which ensures sufficiently high regularity of the deformation field, and the additional nonlinear constraint. This allows us to integrate this new approach without much effort into existing methods.

Performing shape optimization now corresponds to solving the optimal control problem with control c. To test the formulation numerically, we focus on shape optimization for the steady-state Stokes flow; see, e.g., [28]. Figure 1.1 illustrates the geometrical configuration that we use as reference domain. We consider a rectangular domain with an obstacle in the center, which has a smooth boundary Γ_{d}, i.e., the design boundary. On the left boundary of the domain Γ_{in} Dirichlet boundary, conditions and on the right boundary Γ_{out} do-nothing boundary conditions are imposed. On the rest of the boundary, no-slip boundary conditions are imposed. We optimize the shape of the obstacle via the method of mappings such that the drag is minimized. Furthermore, Ω_{d} denotes the domain encircled by Γ_{d}. From a modeling point of view, Ω_{d} represents the aerodynamical object.

Section 2 is devoted to the general formulation of the shape optimization problem. Subsection 2.2 motivates the validity of this approach by theoretical considerations for particular choices for the control-to-deformation mapping. Section 3 presents the application of the abstract framework to the Stokes flow example. An algorithmic realization for solving this optimization problem is given in subsection 3.4. Numerical results in subsection 3.6 show the performance of the different strategies.

2. Shape optimization problem in function space. Let $\Omega \subset \mathbb{R}^d$. We consider the following optimization problem:

$$\begin{aligned} &\min_{c \in D_{\mathrm{ad}}} j(\tau) + \frac{\alpha}{2}\|c\|_X^2 \\ &\text{s.t. } \tau = \mathrm{id} + w, \\ &\qquad g(w) = 0, \\ &\qquad w = S(c), \end{aligned} \tag{2.1}$$

where $g(w)$ represents geometric constraints. The design parameter is denoted by c, and the corresponding transformation is defined via $\tau := \mathrm{id} + w$. Moreover, $D_{\mathrm{ad}} \subset X \hookrightarrow L^2(\Gamma_{\mathrm{d}})$ and S are chosen such that the following assumption holds true:

A1 There exists $\eta > 0$ and an open neighborhood U of Ω such that for all admissible controls $c \in D_{\mathrm{ad}}$, there exists a $\mathcal{C}^1$-diffeomorphism $F : U \to U$ such that $F|_\Omega = \mathrm{id} + S(c)$ and $DF(x)$ has a condition number bounded by η for all $x \in U$.

Assumption A1 ensures that $\mathrm{id} + w$ is the restriction of a $\mathcal{C}^1$-diffeomorphism that maps an open neighborhood of Ω to itself and implies the following lemma.

LEMMA 2.1. *Let $\Omega \subset \mathbb{R}^d$, $d \in \{2, 3\}$, be a smooth domain and assumption* A1 *be fulfilled. Then $(\mathrm{id} + S(c))(\Omega)$ is a Lipschitz domain (even a $\mathcal{C}^1$-domain) for all admissible $c \in D_{\mathrm{ad}}$.*

Proof. Follows directly from [19, Thm. 4.1]. ∎

A second useful requirement can be the one-to-one correspondence between shapes and controls:

A2 Let $c_1, c_2 \in D_{\mathrm{ad}}$. Then $(\mathrm{id} + S(c_1))(\Omega) = (\mathrm{id} + S(c_2))(\Omega)$ if and only if $c_1 = c_2$ a.e.

Remark 2.2. Assumption A2 is not necessary from a modeling perspective; however, it is reasonable from an optimization point of view. Transformations that only change the interior of the domain but not its boundary or transformations that only tangentially move the boundary do not change the domain and therefore, in the absence of regularization or with small regularization parameters, also not (significantly) the objective function value. This has an impact on the performance of optimization algorithms. We give an example. Assume $\tau(\Omega)$ is such that $B_1(0) \subset \tau(\Omega)$. Let $t_1 > 0$ be sufficiently small such that the continuously differentiable function $\varphi_t : \mathbb{R} \to \mathbb{R}$,

$$\varphi_t(\xi) := \begin{cases} 1 + t\xi^2(1-\xi^2)^2 & \text{for } \xi \in (0,1), \\ 1 & \text{else,} \end{cases}$$

fulfills $(\varphi_t(\xi)\xi)' > 0$ for all $t \in I := [0, t_1)$ (since for bijectivity we need $\|x\| > \|y\|$, then $\|T(t)(x)\| > \|T(t)(y)\|$, where $T(t)(x)$ is defined below). Define

$$T(t)(x) := \varphi_t(\|x\|)x,$$

and set $\theta(t) = T(t) \circ \tau$. Then there holds $\theta(0) = \tau$ and, for $t \in I$,

$$\frac{d}{dt}\theta(t)(x) = v(x) := \begin{cases} (\|\tau(x)\|^2(1-\|\tau(x)\|^2)^2)\tau(x) & \text{for } x \in B_1(0), \\ 0 & \text{else,} \end{cases}$$
$$\frac{d^2}{dt^2}\theta(t)(x) = 0.$$

Since, by construction, $\theta(t)(\Omega) = \tau(\Omega)$ for all $t \in I$, it holds $j(\theta(t)) = j(\tau)$ for all $t \in I$ and hence

$$0 = \frac{d}{dt} j(\theta(t))|_{t=0} = \langle j'(\theta(0)), \frac{d}{dt}\theta(0)\rangle = \langle j'(\tau), v\rangle,$$
$$0 = \frac{d^2}{dt^2} j(\theta(t))|_{t=0} = j''(\theta(0))[\frac{d}{dt}\theta(0), \frac{d}{dt}\theta(0)] + \langle j'(\tau), \frac{d^2}{dt^2}\theta(0)\rangle = j''(\tau)[v, v].$$

We thus see that j has curvature 0 along v at τ. There are many other such vector fields along which j has zero curvature. This generates difficulties for Newton's method since the Hessian is not positive definite (if $j''(\tau)$ is positive semidefinite, then v is in the null space of $j''(\tau)$ and thus $j''(\tau)$ is singular).

The assumption motivates to consider scalar-valued functions on the design boundary as control.

2.1. On the choice of D_{ad} and S. Inspired by [16, Lem. 4], we present sufficient conditions for assumption A1 to be fulfilled.

LEMMA 2.3. *Let $d \in \{2, 3\}$, Ω be a bounded Lipschitz domain, and $\eta_1 \in (0, 1)$. Furthermore, let X, Y be Banach spaces such that $Y \hookrightarrow \mathcal{C}^1(\overline{\Omega})^d$, and assume that $S : X \to Y$ is linear and continuous. Then there exists $\eta_2 > 0$ such that for*

$$D_{\mathrm{ad}} \coloneqq \{c \in X \ : \ \det(D(\mathrm{id} + S(c))) \geq \eta_1, \ \|c\|_X \leq \eta_2\},$$

assumption A1 *holds true.*

Proof. Let $c \in D_{\mathrm{ad}}$ and $\tau_c : \Omega \to \tau_c(\Omega)$, $\tau_c \coloneqq \mathrm{id} + S(c)$. We know that $S(c) \in Y$, which embeds into $\mathcal{C}^1(\overline{\Omega})^d$. Moreover, there exists a constant $C_S > 0$ such that

$$\|S(c)\|_{\mathcal{C}^1(\overline{\Omega})^d} \leq C_S \|x\|_X \tag{2.2}$$

for all $c \in D_{\mathrm{ad}}$.

In order to fulfill assumption A1, we have to be able to extend τ_c to a $\mathcal{C}^1$-diffeomorphism $F : U \to U$, where U is an open neighborhood of $\overline{\Omega}$.

By [6, Thm. 2.74, eq. (2.145)] for $k \in \mathbb{N}_0$, there exists an extension operator $\mathrm{Ext} : \mathcal{C}(\overline{\Omega}) \to \mathcal{C}(\mathbb{R}^d)$ such that $\mathrm{Ext}(\mathcal{C}^\ell(\overline{\Omega})) \subset \mathcal{C}^\ell(\mathbb{R}^d)$ for all $\ell \in \{0, \dots, k\}$ and such that there exists $\tilde{C} > 0$ with

$$\max_{|\alpha|=\ell} \sup_{x \in \mathbb{R}^n} |D^\alpha \mathrm{Ext}(f)(x)| \leq \tilde{C} \|f\|_{\mathcal{C}^\ell(\overline{\Omega})} \quad \forall f \in \mathcal{C}^\ell(\overline{\Omega})$$

for all $\ell \in \{0, \dots, k\}$. Hence, there exists an extension $\tilde{w}$ of $S(c)$ and a constant $C_{\mathrm{ext}} > 0$ such that

$$\|\tilde{w}\|_{\mathcal{C}^1(\mathbb{R}^d)^d} \leq C_{\mathrm{ext}} \|S(c)\|_{\mathcal{C}^1(\overline{\Omega})^d} \tag{2.3}$$

and $\tilde{w}|_\Omega = S(c)$. We choose $\alpha > 0$ and set $U \coloneqq B_\alpha(\Omega)$. Let $\varphi \coloneqq 1_{B_{\frac{\alpha}{2}}(\Omega)} * \psi$ be the convolution of the indicator function $1_{B_{\frac{\alpha}{2}}(\Omega)}$ of $B_{\frac{\alpha}{2}}(\Omega)$ and a mollifier $\psi \in \mathcal{C}^\infty(\mathbb{R}^d)$

such that $\int_{\mathbb{R}^d} \psi dx = 1$ and $\operatorname{supp}(\psi) \subset B_{\frac{\alpha}{4}}(0)$. Thus, $\varphi \in \mathcal{C}^\infty(\mathbb{R}^d)$, and there exists $C_\alpha > 0$ such that

$$\|\varphi\|_{\mathcal{C}^1(\mathbb{R}^d)} \leq C_\alpha. \tag{2.4}$$

Define $F := \mathrm{id} + \tilde{w}\varphi$, which is an element of $\mathcal{C}^1(\mathbb{R}^d)^d$ such that $F(U) \subset U$ and $F(x) = x$ for all $x \in \mathbb{R}^d \setminus U$. By (2.4), (2.3), (2.2), and the definition of D_{ad}, there exists $C > 0$ such that

$$\|\tilde{w}\varphi\|_{\mathcal{C}^1(\mathbb{R}^d)^d} \leq C C_{\mathrm{ext}} C_\alpha C_S \eta_2. \tag{2.5}$$

Furthermore, choosing η_2 sufficiently small, there exists a constant $\tilde{C} > 0$ such that

$$\begin{aligned} \det(DF(x)) &\geq 1 - \|\det(DF(x)) - \det(D\,\mathrm{id}(x))\|_{C(\mathbb{R}^d)} \\ &\geq 1 - \tilde{C}\|\tilde{w}\varphi\|^d_{\mathcal{C}^1(\mathbb{R}^d)^d} \geq 1 - \tilde{C}(C C_{\mathrm{ext}} C_\alpha C_S \eta_2)^d =: \tilde{\eta}_1 > 0 \end{aligned} \tag{2.6}$$

for all $x \in \mathbb{R}^d$, where we used (2.5) and that the determinant is a polynomial of degree d in the entries of the matrix where d denotes the dimension.

$F : \mathbb{R}^d \to \mathbb{R}^d$ is norm-coercive, i.e., $\|F(x)\| \to \infty$ for $\|x\| \to \infty$, and continuously differentiable with invertible derivative since $\det(DF(x)) \geq \tilde{\eta}_1 > 0$ for all $x \in \mathbb{R}^d$. Hence, due to [21, Thm. 1.2], $F : \mathbb{R}^d \to \mathbb{R}^d$ is a diffeomorphism. Thus, by definition of F, $F : U \to U$ is a diffeomorphism.

In addition, by (2.5), there exists a constant $C > 0$ such that $\|DF\|_{\mathcal{C}(\overline{U})^{d\times d}} \leq \|F\|_{\mathcal{C}^1(\overline{U})^d} \leq C$ uniformly on D_{ad}. From this, uniform boundedness of the largest eigenvalue of DF on U and D_{ad} follows. By (2.6), $\det(DF(x)) \geq \tilde{\eta}_1 > 0$ uniformly on D_{ad} and U. Since the determinant corresponds to the product of the eigenvalues, the smallest eigenvalue of DF is uniformly bounded from below by a constant larger than 0. This yields assumption A1. ∎

Remark 2.4. Alternatively, if one provides a mesh for the holdall domain U (e.g., $U = \Omega \cup \Omega_{\mathrm{d}} \cup \Gamma_{\mathrm{d}}$ in the example shown in Figure 1.1), w and the constraint $\det(D(\mathrm{id} + w))$ can be defined on U. Doing so, the smallness assumption on η_2 is not needed since we can use the trivial extension of $S(c)$ by zero. Furthermore, Lemma 2.3 can also be extended to nonlinear S if one adds another Banach space $\tilde{X}$. This leads to the following lemma, which does not require the deformations to be sufficiently close to identity.

LEMMA 2.5. *Let $d \in \{2, 3\}$, Ω, U be bounded Lipschitz domains with $\Omega \subset U$, $\eta_1 \in (0, 1)$, and $\eta_2 > 0$. Furthermore, let X, $\tilde{X}$, Y be Banach spaces such that $Y \hookrightarrow \mathcal{C}^1_c(U)^d$, let X be compactly embedded into $\tilde{X}$, and assume that $S : X \to Y$ is continuous with $S(0) = 0$ and that S can be extended to a continuous mapping $S : \tilde{X} \to \mathcal{C}^1(\overline{U})^d$. Then, for*

$$D_{\mathrm{ad}} \coloneqq \{c \in X \ : \ \det(D(\mathrm{id} + S(c))) \geq \eta_1, \ \|c\|_X \leq \eta_2\},$$

assumption A1 *holds true.*

Proof. The proof is very similar to the proof of Lemma 2.3. However, the extension becomes trivial since one can extend $S(c)$ by 0 onto $\mathbb{R}^d \setminus U$. Let $c \in D_{\mathrm{ad}}$. The condition $S(0) = 0$ ensures that D_{ad} is nonempty. Since $S(c) \in \mathcal{C}^1_c(U)^d$, $F : U \to U, F(x) := (\mathrm{id} + S(c))(x)$ can be extended to $\tilde{F} : \mathbb{R}^d \to \mathbb{R}^d$, setting $\tilde{F}(x) = x$ for all $x \in \mathbb{R}^d \setminus U$ and $\tilde{F}(x) = F(x)$ for all $x \in U$. $\tilde{F}$ is norm-coercive and continuously differentiable with invertible derivative since $\det(D\tilde{F}(x)) \geq \eta_1 > 0$ for all $x \in U$.

Hence, due to [21, Thm. 1.2], $\tilde{F}$ is a diffeomorphism. Thus, $F : U \to U$ is a diffeomorphism. By continuity of $S : \tilde{X} \to \mathcal{C}^1(\overline{U})^d$ and compactness of $\{c \in X \ : \ \|c\|_X \leq \eta_2\}$ in $\tilde{X}$, we obtain boundedness of $\|S(c)\|_{\mathcal{C}^1(\overline{U})^d}$ uniformly on D_{ad}. Hence, $\|DF\|_{\mathcal{C}(\overline{U})^d}$ is bounded uniformly on D_{ad}, which implies that the largest eigenvalue is bounded uniformly on D_{ad} and U. Uniform boundedness of the smallest eigenvalue from below holds by $\det(D(\mathrm{id}+S(c))) \geq \eta_1$, the bounds on the largest eigenvalue, and the fact that the determinant corresponds to the product of the eigenvalues. Hence, assumption A1 holds. ∎

2.2. Different strategies for the choice of S. The requirements in the previous section allow for different choices of S. We will present three strategies for which assumption A1 is satisfied. For the first one, we additionally prove that assumption A2 holds. To avoid technicalities, we consider a smooth domain Ω with boundary Γ. Furthermore, we assume that $\Gamma \setminus \Gamma_{\mathrm{d}} \neq \emptyset$. In agreement with the numerical examples considered in section 3.6, we further assume Γ_{d} to be a compact manifold without boundary. The outer unit normal vector field is denoted by n. We consider

- the Laplace–Beltrami equation on Γ_{d}
$$-\Delta_{\Gamma_{\mathrm{d}}} b + b = f \quad \text{on } \Gamma_{\mathrm{d}}$$
with a solution operator that maps f to b, denoted by $S_{\Gamma_{\mathrm{d}}}$ in the scalar-valued case and by $S^d_{\Gamma_{\mathrm{d}}}$ in the vector-valued case;
- the elliptic equation
$$\begin{aligned} -\Delta z &= 0 \quad \text{in } \Omega, \\ z &= 0 \quad \text{on } \Gamma \setminus \Gamma_{\mathrm{d}}, \\ \nabla z \cdot n &= b \quad \text{on } \Gamma_{\mathrm{d}} \end{aligned}$$
with solution operator S_Ω that maps a scalar-valued b to a scalar-valued z;
- the elliptic equation
$$\begin{aligned} -\operatorname{div}(Dz + Dz^\top) &= 0 \quad \text{in } \Omega, \\ z &= 0 \quad \text{on } \Gamma \setminus \Gamma_{\mathrm{d}}, \\ \nabla z \cdot n &= b \quad \text{on } \Gamma_{\mathrm{d}} \end{aligned}$$
with solution operator S^d_Ω that maps a vector-valued b to a vector-valued z;

and the following strategies for S:

S1 We choose $S(c) := S_\Omega(S_{\Gamma_{\mathrm{d}}}(c))n_{\mathrm{ext}}$, where n_{ext} denotes an extension of the outer unit normal vector field n to Ω. Strategy 1 only allows for displacements of Γ_{d} along normal directions.

S2 As strategy 2, we choose $S(c) := S^d_\Omega(S_{\Gamma_{\mathrm{d}}}(c)n)$.

S3 For strategy 3, we define $S(c) := S^d_\Omega(S^d_{\Gamma_{\mathrm{d}}}(cn))$.

Remark 2.6. We are not restricted to these strategies. Strategies S1–S3 are discussed and numerically investigated in this work to demonstrate the advantages and limitations of the proposed approach. Strategies S2 and S3 are motivated by the approach used in [34]. Instead of directly optimizing a vector-valued function on the design boundary, a scalar-valued function is mapped to a vector-valued function with higher regularity involving a boundary operator and the normal vectors to comply with Remark 2.2 and the requirements of assumption A1. Strategy S1 reflects the Hadamard–Zolésio structure theorem using similar elliptic equations. Note that there might be better strategies that move the boundary in normal direction; however, we will use strategy S1 to demonstrate the main advantage numerically: Independently of the choice of S as long as assumption A1 is satisfied, the nonlinear determinant

constraint becomes active or violated before the mesh becomes computationally infeasible, which prevents the algorithm from not converging due to mesh degeneration. A smaller parameter η_1 (and fixed η_2) allows for a higher degree of mesh degeneracy. An optimal solution with active determinant constraint indicates that using another strategy or remeshing and restarting the optimization process might yield better solutions. Keeping this in mind also motivates that the choice of n_{ext} is crucial for strategy S1. The main limitation is the regularity requirement on the transformations that fulfill assumption A1, which we mentioned in the introduction.

Representatively, we show that assumption A1 holds for strategy S1. It is straightforward to adapt this argumentation for strategies S2 and S3. In addition, we show that assumption A2 holds for strategy S1. Motivated by this result, we also choose a scalar-valued function on the design boundary as control for strategies S2 and S3 without proving that asspumtion A2 holds for these strategies.

Displacement along normal directions. We consider $S(c) \coloneqq S_\Omega(S_{\Gamma_\mathrm{d}}(c))n_{\text{ext}}$, where n_{ext} is a smooth extension of the outer unit normal vectors to Ω. Using Lemma 2.3, we prove that assumptions A1 and A2 are fulfilled if n_{ext} and the Banach space X are chosen in an appropriate way; see Lemma 2.9. To this end, we recall well-known results for the elliptic solution operators.

LEMMA 2.7 (elliptic equation on compact manifolds without boundary). *Let $s \geq -1$, Γ_d be a smooth and compact Riemannian manifold without boundary, and consider the system*

$$-\Delta_{\Gamma_\mathrm{d}} b + b = f \tag{2.7}$$

on Γ_d, where $\Delta_{\Gamma_\mathrm{d}}$ denotes the Laplace–Beltrami operator on Γ_d. Then, for any $f \in H^s(\Gamma_\mathrm{d})$, there exists a unique solution $b \in H^{s+2}(\Gamma_\mathrm{d})$, and the corresponding solution operator $S_{\Gamma_\mathrm{d}} : H^s(\Gamma_\mathrm{d}) \to H^{s+2}(\Gamma_\mathrm{d})$ is continuous.

Proof. See [40, pp. 362–363]. ∎

Since Γ_d is closed and has positive distance from $\Gamma \setminus \Gamma_\mathrm{d}$, classical results for the Dirichlet and Neumann boundary value problem also hold for the mixed boundary value problem in our setting, whereas it gets more involved when the positive distance assumption is not fulfilled; see, e.g., [26].

LEMMA 2.8. *Let $\Omega \subset \mathbb{R}^d$, $d \in \{2, 3\}$, be a smooth domain and $\Gamma_\mathrm{d} \subset \Gamma$ be a closed subset of the boundary such that $\Gamma \setminus \Gamma_\mathrm{d} \neq \emptyset$. Assume that Γ_d and $\Gamma \setminus \Gamma_\mathrm{d}$ have positive distance. Let $s \geq 2$. Consider the following system:*

$$\begin{aligned} -\Delta z &= 0 \quad \text{in } \Omega, \\ z &= 0 \quad \text{on } \Gamma \setminus \Gamma_\mathrm{d}, \\ \nabla z \cdot n &= b \quad \text{on } \Gamma_\mathrm{d}. \end{aligned} \tag{2.8}$$

Then, for every $b \in H^{s-\frac{3}{2}}(\Gamma_\mathrm{d})$, there exists a unique solution $z \in H^s(\Omega)$, and the corresponding solution operator $S_\Omega : H^{s-\frac{3}{2}}(\Gamma_\mathrm{d}) \to H^s(\Omega)$ is continuous.

Proof. See [27, p. 188, Rem. 7.2]. ∎

These two lemmas imply that assumptions A1 and A2 are fulfilled for the choice $S(\cdot) = \tilde{S}(\cdot)n_{\text{ext}}$, $\tilde{S} = S_\Omega \circ S_{\Gamma_\mathrm{d}}$ and $X = L^2(\Gamma_\mathrm{d})$ as the following lemma shows.

LEMMA 2.9. *Let $\Omega \subset \mathbb{R}^d$, $d \in \{2, 3\}$, be a bounded $\mathcal{C}^\infty$-domain and $X = L^2(\Gamma_\mathrm{d})$. Let $\tilde{S}(c) \coloneqq S_\Omega(S_{\Gamma_\mathrm{d}}(c))$ for all $c \in X$. Then there exists $\eta_2 > 0$ such that assumptions* A1 *and* A2 *are fulfilled for $S(\cdot) = \tilde{S}(\cdot)n_{\text{ext}}$ for D_{ad} chosen as in Lemma* 2.3.

Proof. By Lemmas 2.7 and 2.8, $S_\Omega(S_\Gamma(X)) \subset H^{\frac{7}{2}}(\Omega)$, which embeds into $\mathcal{C}^1(\overline{\Omega})$. Thus, S fulfills the requirements of Lemma 2.3, and assumption A1 holds. Let $c_1, c_2 \in X$ and $S(c_1)(\Omega) = S(c_2)(\Omega)$. Then $\tilde{S}(c_1)|_{\Gamma_\mathrm{d}} = \tilde{S}(c_2)|_{\Gamma_\mathrm{d}}$. Linearity and well-definedness of the Neumann-to-Dirichlet map for the elliptic equations (2.8) (see, e.g., [23, sect. 2]) implies $S_{\Gamma_\mathrm{d}}(c_1) = S_{\Gamma_\mathrm{d}}(c_2)$. Thus, due to injectivity of S_{Γ_d}, $c_1 = c_2$ a.e., and assumption A2 is fulfilled. ∎

3. Example: Stokes flow. We now apply (1.3) to minimize the drag of an obstacle in steady-state Stokes flow; see Figure 1.1. The optimization problem is given by

$$
\begin{aligned}
&\min_{c\in L^2(\Gamma_\mathrm{d})} \frac{1}{2}\int_{\tau(\Omega)} (Dv : Dv)dx + \frac{\alpha}{2}\|c\|^2_{L^2(\Gamma_\mathrm{d})} \\
&\text{s.t.} \begin{cases} -\Delta v + \nabla p = 0 & \text{in } \tau(\Omega), \\ \operatorname{div}(v) = 0 & \text{in } \tau(\Omega), \\ v = 0 & \text{on } \tau(\Gamma_\mathrm{d}) \cup \Gamma_\mathrm{ns}, \\ v = v_\mathrm{in} & \text{on } \Gamma_\mathrm{in}, \\ (Dv - pI)n = 0 & \text{on } \Gamma_\mathrm{out}, \end{cases} \\
&\quad \tau = \mathrm{id} + w, \\
&\quad w = S(c), \\
&\quad g(w) = 0, \\
&\quad \|c\|_X \le \eta_2, \\
&\quad \det(D\tau) \ge \eta_1 \quad \text{in } \Omega.
\end{aligned} \tag{3.1}
$$

Here, v denotes the fluid velocity, p the fluid pressure, and v_in nonhomogeneous Dirichlet boundary conditions on Γ_in, and S is chosen such that the trace $S(c)|_{\Gamma_\mathrm{ns}\cup\Gamma_\mathrm{in}\cup\Gamma_\mathrm{out}} = 0$ for all admissible $c \in L^2(\Gamma_\mathrm{d})$. In order to exclude trivial solutions, we add geometric constraints $g(w) = 0$ to the optimization problem (3.1), which are further discussed in subsection 3.2.

3.1. Algorithmic realization. We want to use state-of-the-art finite element toolboxes to solve the optimization problem. This can, e.g., be realized by penalizing the violation of the inequality constraints. The additional norm constraint on c is approximated by a norm penalization and a possible adjustment of α. Hence, we obtain the equality constrained optimization problem

$$
\begin{aligned}
&\min_{c\in L^2(\Gamma_\mathrm{d})} \frac{1}{2}\int_{\tau(\Omega)} (Dv : Dv)dx + \frac{\alpha}{2}\|c\|^2_{L^2(\Gamma_\mathrm{d})} + \frac{\gamma_1}{2}\|(\eta_1 - \det(D\tau))_+\|^2_{L^2(\Omega)} \\
&\text{s.t.} \begin{cases} -\Delta v + \nabla p = 0 & \text{in } \tau(\Omega), \\ \operatorname{div}(v) = 0 & \text{in } \tau(\Omega), \\ v = 0 & \text{on } \tau(\Gamma_\mathrm{d}) \cup \Gamma_\mathrm{ns}, \\ v = v_\mathrm{in} & \text{on } \Gamma_\mathrm{in}, \\ (Dv - pI)n = 0 & \text{on } \Gamma_\mathrm{out}, \end{cases} \\
&\quad \tau = \mathrm{id} + w, \\
&\quad w = S(c), \\
&\quad g(w) = 0,
\end{aligned} \tag{3.2}
$$

where $\gamma_1 > 0$ denotes a penalization parameter and $(\cdot)_+ \coloneqq \max(0, \cdot)$. In order to simplify the notation, we will use the notation $J_\tau \coloneqq \det(D\tau)$ in the following. The

first-order necessary optimality conditions of (3.2) yield a system of nonlinear, coupled PDEs; see subsection 3.4.

Algorithm 3.1 Optimization strategy.

Require: $0 < \alpha_{\text{target}} \leq \alpha_{\text{init}}$, $0 < \alpha_{\text{dec}} < 1$, $0 \leq \gamma_1$, $0 < \eta_1$

1: $k \leftarrow 0$, $\alpha_k \leftarrow \alpha_{\text{init}}$, $c_k \leftarrow 0$
2: **while** $\alpha_k \geq \alpha_{\text{target}}$ **do**
3: Solve (3.2) iteratively with initial point c_k and solution c
4: $\alpha_{k+1} \leftarrow \alpha_{\text{dec}}\alpha_k$, $c_{k+1} \leftarrow c$
5: $k \leftarrow k + 1$
6: **end while**

In principle, one solution of this nonlinear system of PDEs leads to the desired optimal solution for a given α. From a computational point of view, yet, the solvability of this system with semismooth Newton methods depends on a proper initialization. Therefore, we solve (3.2) for a sequence of decreasing regularization parameters α (see Algorithm 3.1) until a desired α_{target} is reached. Thus, the solution of one optimization problem can be utilized as initialization for the subsequent one. The following sections are devoted to the explicit derivation of the optimality system of (3.2) in a weak form; see subsection 3.4. Therefore, the geometrical constraints (subsection 3.2) are discussed, and the different strategies for the control-to-transformation mapping S are investigated in more detail.

3.2. Geometrical constraints. For shape optimization in the context of fluid dynamics, it is necessary to fix the barycenter and volume of the obstacle Ω_{d}. This is to avoid design improvements by moving it to the walls of the flow tunnel or shrinking it to a point. In the following, we use the symbol $\hat{\cdot}$ to refer to the deformed geometrical entity in terms of the mapping τ. For instance, the deformed reference domain is then denoted by $\hat{\Omega} \coloneqq \tau(\Omega)$.

Let U be the holdall domain and the obstacle $\hat{\Omega}_{\text{d}} = U \setminus \hat{\Omega}$. Further, let

$$\text{vol}(\hat{\Omega}_{\text{d}}) = \int_{\hat{\Omega}_{\text{d}}} 1 \, d\hat{x}, \quad \text{bc}(\hat{\Omega}_{\text{d}}) = \frac{1}{\text{vol}(\hat{\Omega}_{\text{d}})} \int_{\hat{\Omega}_{\text{d}}} \hat{x} \, d\hat{x} \tag{3.3}$$

denote the volume and barycenter of the obstacle.

In the numerical implementation, we work with the corresponding boundary integral formulations instead in order to achieve a better sparsity in the linearized systems. Alternatively, it is also possible to work with the domain integral formulations as, for instance, in [31]. Let $\hat{n} : \hat{\Gamma}_{\text{d}} \to \mathbb{R}^d$ be the unit normal on $\hat{\Gamma}_{\text{d}}$ and $f \in L^1(\hat{\Gamma}_{\text{d}})$. According to [39, Props. 2.47 and 2.48], we have

$$\int_{\hat{\Gamma}_{\text{d}}} \hat{f} \, ds(\hat{x}) = \int_{\Gamma_{\text{d}}} f \|J_\tau (D\tau)^{-\top} n\|_2 \, ds(x). \tag{3.4}$$

Furthermore, the normal vector on the deformed boundary $\hat{\Gamma}_{\text{d}}$ is given in terms of the normal vector n on the boundary of the reference domain Γ_{d} as

$$\hat{n} \circ \tau = \frac{1}{\|(D\tau)^{-\top} n\|_2} (D\tau)^{-\top} n. \tag{3.5}$$

Applying (3.4) and (3.5) to (3.3), we obtain

$$\begin{aligned}\operatorname{vol}(\hat{\Omega}) &= \int_{\hat{\Omega}} 1\, d\hat{x} = \frac{1}{d}\int_{\hat{\Gamma}_\mathrm{d}} \hat{x}^\top \hat{n}\, d\hat{s}(\hat{x}) \\ &= \frac{1}{d}\int_{\Gamma_\mathrm{d}} (x+w)^\top (\hat{n}\circ\tau)\|J_\tau (D\tau)^{-\top} n\|_2\, ds(x) \\ &= \frac{1}{d}\int_{\Gamma_\mathrm{d}} (x+w)^\top (D\tau)^{-\top} n |J_\tau|\, ds(x)\end{aligned} \tag{3.6}$$

for the volume and

$$\begin{aligned}(\mathrm{bc}(\hat{\Omega}_\mathrm{d}))_i &= \frac{1}{\operatorname{vol}(\hat{\Omega}_\mathrm{d})}\int_{\hat{\Omega}_\mathrm{d}} \hat{x}_i\, d\hat{x} = \frac{1}{\operatorname{vol}(\hat{\Omega}_\mathrm{d})}\int_{\hat{\Gamma}_\mathrm{d}} \frac{1}{2} x_i^2 \hat{n}_i\, d\hat{s}(\hat{x}) \\ &= \frac{1}{2\operatorname{vol}(\hat{\Omega}_\mathrm{d})}\int_{\Gamma_\mathrm{d}} (x_i+w_i)^2 \frac{1}{\|(D\tau)^{-\top} n\|_2}\left[(D\tau)^{-\top} n\right]_i \|J_\tau (D\tau)^{-\top} n\|_2\, ds(x) \\ &= \frac{1}{2\operatorname{vol}(\hat{\Omega}_\mathrm{d})}\int_{\Gamma_\mathrm{d}} (x_i+w_i)^2 \left[(D\tau)^{-\top} n\right]_i |J_\tau|\, ds(x)\end{aligned} \tag{3.7}$$

for the ith component of the barycenter. Hence, choosing the desired barycenter to be $0 \in \mathbb{R}^d$ without loss of generality and $J_\tau \geq \eta_1 > 0$, we obtain the constant volume condition

$$\int_{\Gamma_\mathrm{d}} (x+w)^\top (D\tau)^{-\top} n J_\tau - x^\top n\, ds(x) = 0, \tag{3.8}$$

and the barycenter condition reduces to

$$\int_{\Gamma_\mathrm{d}} (x_i+w_i)^2 \left[(D\tau)^{-\top} n\right]_i J_\tau\, ds(x) = 0. \tag{3.9}$$

In the following, we shortly write ds instead of $ds(x)$. Also note that the absolute value for J_τ is omitted due to the condition $J_\tau \geq \eta_1$ in the optimization problem (3.1).

3.3. On the different strategies for S. In section 2, we discuss different choices of the operator S. In all strategies, the operator S involves solving an equation of the Laplace–Beltrami type and an elliptic extension equation. Thus, the scalar-valued control variable c is mapped from the shape boundary Γ_d to a vector-valued displacement field w in Ω. The major difference in the considered strategies is when the variable becomes vector-valued. We thus consider a mapping given by

$$c \overset{\text{i)}}{\mapsto} b \overset{\text{ii)}}{\mapsto} z \overset{\text{iii)}}{\mapsto} w, \tag{3.10}$$

where i) is realized via the Laplace–Beltrami solution operator on Γ_d and ii) via a solution operator for an elliptic equation in Ω. Depending on when the variables become vector-valued, z plays the role of w.

First strategy (S1). The corresponding weak formulation for the operators S_{Γ_d} and S_Ω (step i) and step ii), respectively) is given by

$$\int_\Omega \nabla z \cdot \nabla \psi_z\, dx = \int_{\Gamma_\mathrm{d}} b\psi_z\, ds, \tag{3.11}$$

$$\int_{\Gamma_\mathrm{d}} b\psi_b + \nabla_{\Gamma_\mathrm{d}} b \cdot \nabla_{\Gamma_\mathrm{d}} \psi_b\, ds = \int_{\Gamma_\mathrm{d}} c\psi_b\, ds \tag{3.12}$$

for all suitable test functions ψ_z and ψ_b. Since our intention is to formulate everything suitable for weak-form languages of the major FEM toolboxes, we realize step iii) in the form

$$\int_\Omega w \cdot \psi_n \, dx = \int_\Omega z n_{\text{ext}} \cdot \psi_n \, dx \tag{3.13}$$

for all suitable test functions ψ_n.

Second strategy (S2). The elliptic extension equation in step ii) (corresponding to the operator S_Ω^d) is defined to be vector-valued, which then allows to omit step iii). This reads in weak formulation as

$$\int_\Omega (Dw + Dw^\top) : D\psi_w \, dx = \int_{\Gamma_\text{d}} bn \cdot \psi_w \, ds \tag{3.14}$$

for all ψ_w and replaces (3.11) compared to strategy S1. Note that we use the symmetrized derivative $(Dw + Dw^\top)$ in (3.14), which corresponds to solving the Lamé system with Lamé parameters $\mu = 1$ and $\lambda = 0$ and is found to lead to better mesh qualities after deformation compared to using Dw instead. With our approach, it is not required to tune these parameters, contrary to previous approaches; see, e.g., [34, 7]. This is later substantiated with numerical results in Figure 3.2. Furthermore, (3.13) is dropped from the system.

Third strategy (S3). In a third possible strategy, the scalar-valued control c is immediately mapped to a vector-valued b in step i) by the vector-valued Laplace–Beltrami solution operator. The scalar-valued control c enters as a scaling of n, and then a vector-valued Laplace–Beltrami type of equation is considered. The corresponding vector-valued solution operator $S_{\Gamma_\text{d}}^d$ is given in the following weak formulation for all test functions ψ_b by

$$\int_{\Gamma_\text{d}} b \cdot \psi_b + D_{\Gamma_\text{d}} b : D_{\Gamma_\text{d}} \psi_b \, ds = \int_{\Gamma_\text{d}} cn \cdot \psi_b \, ds. \tag{3.15}$$

Consequently, the operator S_Ω^d is similar to the one in strategy S2 and, compared to (3.14), only differs on the right-hand side of the weak formulation

$$\int_\Omega (Dw + Dw^\top) : D\psi_w \, dx = \int_{\Gamma_\text{d}} b \cdot \psi_w \, ds. \tag{3.16}$$

3.4. Optimality system. We present the optimality system for strategy S3. Strategies S1 and S2 can be handled analogously. We consider the function spaces

$$\begin{aligned}
&W = \{w \in H^{\frac{7}{2}}(\Omega)^d \ : \ w|_{\Gamma \setminus \Gamma_\text{d}} = 0\}, \quad W_0 = H_0^{\frac{7}{2}}(\Omega)^d, \\
&V = \{v \in H^1(\Omega)^d \ : \ v|_{\Gamma_\text{d} \cup \Gamma_\text{ns}} = 0, v|_{\Gamma_\text{in}} = v_\text{in}\}, \\
&V_0 = \{v \in H^1(\Omega)^d \ : \ v|_{\Gamma_\text{d} \cup \Gamma_\text{ns}} = 0, v|_{\Gamma_\text{in}} = 0\}, \\
&\Pi = L_0^2(\Omega) := \{p \in L^2(\Omega) \ : \ \int_\Omega p(x) dx = 0\}, \qquad B = H^2(\Gamma_\text{d})^d.
\end{aligned}$$

Using that the weak formulation of the transformed Stokes equations is given in terms of test functions ψ_v and ψ_p by

$$\begin{aligned}
\int_\Omega \left(Dv(D\tau)^{-1}\right) : \left(D\psi_v(D\tau)^{-1}\right) J_\tau \, dx - \int_\Omega p \operatorname{Tr}\left(D\psi_v(D\tau)^{-1}\right) J_\tau \, dx \\
+ \int_\Omega \psi_p \operatorname{Tr}(Dv(D\tau)^{-1}) J_\tau \, dx = 0,
\end{aligned} \tag{3.17}$$

the Lagrangian for the energy dissipation minimization problem of a Stokes flow around an obstacle with fixed volume and barycenter is given by

$$
\begin{aligned}
(3.18)\quad & \mathcal{L}(w,v,p,b,\psi_w,\psi_v,\psi_p,\psi_b,c,\lambda,\mu)\\
&= \frac{1}{2}\int_\Omega \left(Dv(D\tau)^{-1}\right) : \left(Dv(D\tau)^{-1}\right) J_\tau \, dx + \frac{\alpha}{2}\int_{\Gamma_{\mathrm{d}}} c^2 \, ds + \frac{\gamma_1}{2}\int_\Omega ((\eta_1 - J_\tau)_+)^2 \, dx\\
&\quad - \int_\Omega \left(Dv(D\tau)^{-1}\right) : \left(D\psi_v(D\tau)^{-1}\right) J_\tau \, dx + \int_\Omega p \operatorname{Tr}\left(D\psi_v(D\tau)^{-1}\right) J_\tau \, dx\\
&\quad - \int_\Omega \psi_p \operatorname{Tr}(Dv(D\tau)^{-1}) J_\tau \, dx - \int_\Omega (Dw + Dw^\top) : D\psi_w \, dx + \int_{\Gamma_{\mathrm{d}}} b \cdot \psi_w \, ds\\
&\quad - \int_{\Gamma_{\mathrm{d}}} b \cdot \psi_b + D_{\Gamma_{\mathrm{d}}} b : D_{\Gamma_{\mathrm{d}}} \psi_b \, ds + \int_{\Gamma_{\mathrm{d}}} cn \cdot \psi_b \, ds\\
&\quad + \sum_{i=1}^d \mu_i \int_{\Gamma_{\mathrm{d}}} (x_i + w_i)^2 \left((D\tau)^{-\top} n\right)_i J_\tau \, ds + \frac{\lambda}{d}\int_{\Gamma_{\mathrm{d}}} (x+w)^\top (D\tau)^{-\top} n J_\tau - x \cdot n \, ds,
\end{aligned}
$$

where $(\psi_w, \psi_v, \psi_p, \psi_b) \in W_0 \times V_0 \times \Pi \times B$ denotes the adjoint states, $(w, v, p, b) \in W \times V \times \Pi \times B$ the forward states, $c \in L^2(\Gamma_{\mathrm{d}})$ the control, and $\lambda \in \mathbb{R}, \mu \in \mathbb{R}^3$ the Lagrange multipliers.

For the sake of simplicity we write in the following $\mathcal{L}$ for $\mathcal{L}(w, v, p, \psi_w, \psi_v, \psi_p, c, \lambda, \mu)$. Using $((D\tau)^{-1})_w h_w = -(D\tau)^{-1} Dh_w (D\tau)^{-1}$ and $(J_\tau)_w h_w = \operatorname{Tr}((D\tau)^{-1} Dh_w) J_\tau$, the first-order necessary optimality conditions are given by

$$
\begin{aligned}
\mathcal{L}_w h_w = & -\int_\Omega (Dv(D\tau)^{-1}) : (Dv(D\tau)^{-1} Dh_w (D\tau)^{-1}) J_\tau \, dx\\
& + \frac{1}{2}\int_\Omega (Dv(D\tau)^{-1}) : (Dv(D\tau)^{-1}) \operatorname{Tr}((D\tau)^{-1} Dh_w) J_\tau \, dx\\
& - \gamma_1 \int_\Omega (\eta_1 - J_\tau)_+ \operatorname{Tr}((D\tau)^{-1} Dh_w) J_\tau \, dx\\
& + \int_\Omega (Dv(D\tau)^{-1} Dh_w (D\tau)^{-1}) : (D\psi_v (D\tau)^{-1}) J_\tau \, dx\\
& + \int_\Omega (Dv(D\tau)^{-1}) : (D\psi_v (D\tau)^{-1} Dh_w (D\tau)^{-1}) J_\tau \, dx\\
& - \int_\Omega (Dv(D\tau)^{-1}) : (D\psi_v (D\tau)^{-1}) \operatorname{Tr}((D\tau)^{-1} Dh_w) J_\tau \, dx\\
& - \int_\Omega p \operatorname{Tr}(D\psi_v (D\tau)^{-1} Dh_w (D\tau)^{-1}) J_\tau \, dx\\
& + \int_\Omega p \operatorname{Tr}(D\psi_v (D\tau)^{-1}) \operatorname{Tr}((D\tau)^{-1} Dh_w) J_\tau \, dx\\
& + \int_\Omega \psi_p \operatorname{Tr}(Dv(D\tau)^{-1} Dh_w (D\tau)^{-1}) J_\tau \, dx\\
& - \int_\Omega \psi_p \operatorname{Tr}(Dv(D\tau)^{-1}) \operatorname{Tr}((D\tau)^{-1} Dh_w) J_\tau \, dx\\
& - \int_\Omega (Dh_w + Dh_w{}^\top) : D\psi_w \, dx\\
& + \sum_{i=1}^d \mu_i \int_{\Gamma_{\mathrm{d}}} 2(x_i + w_i)(h_w)_i ((D\tau)^{-\top} n)_i J_\tau \, dx
\end{aligned}
\qquad (3.19)
$$

$$
\begin{aligned}
&- \sum_{i=1}^{d} \mu_i \int_{\Gamma_\mathrm{d}} (x_i + w_i)^2 ((D\tau)^{-\top} (Dh_w)^\top (D\tau)^{-\top} n)_i J_\tau \, dx \\
&+ \sum_{i=1}^{d} \mu_i \int_{\Gamma_\mathrm{d}} (x_i + w_i)^2 ((D\tau)^{-\top} n)_i \operatorname{Tr}((D\tau)^{-1} Dh_w) J_\tau \, dx \\
&+ \frac{\lambda}{d} \int_{\Gamma_\mathrm{d}} (x + h_w)^\top (D\tau)^{-\top} n J_\tau \, ds \\
&- \frac{\lambda}{d} \int_{\Gamma_\mathrm{d}} (x + w)^\top (D\tau)^{-\top} (Dh_w)^\top (D\tau)^{-\top} n J_\tau \, ds \\
&+ \frac{\lambda}{d} \int_{\Gamma_\mathrm{d}} (x + w)^\top (D\tau)^{-\top} n \operatorname{Tr}((D\tau)^{-1} Dh_w) J_\tau \, ds = 0,
\end{aligned}
$$

(3.20)

$$
\begin{aligned}
\mathcal{L}_v h_v = &\int_\Omega \left(Dh_v (D\tau)^{-1}\right) : \left(Dv (D\tau)^{-1}\right) J_\tau \, dx \\
&- \int_\Omega \left(Dh_v (D\tau)^{-1}\right) : \left(D\psi_v (D\tau)^{-1}\right) J_\tau \, dx - \int_\Omega \psi_p \operatorname{Tr}(Dh_v (D\tau)^{-1}) J_\tau \, dx = 0,
\end{aligned}
$$

$$
\mathcal{L}_p h_p = \int_\Omega h_p \operatorname{Tr}\left(D\psi_v (D\tau)^{-1}\right) J_\tau \, dx = 0, \tag{3.21}
$$

$$
\begin{aligned}
\mathcal{L}_{\psi_v} h_{\psi_v} = &- \int_\Omega \left(Dv (D\tau)^{-1}\right) : \left(Dh_{\psi_v} (D\tau)^{-1}\right) J_\tau \, dx \\
&+ \int_\Omega p \operatorname{Tr}(Dh_{\psi_v} (D\tau)^{-1}) J_\tau \, dx = 0,
\end{aligned} \tag{3.22}
$$

$$
\mathcal{L}_{\psi_p} h_{\psi_p} = - \int_\Omega h_{\psi_p} \operatorname{Tr}\left(Dv (D\tau)^{-1}\right) J_\tau \, dx = 0, \tag{3.23}
$$

$$
\mathcal{L}_{\psi_w} h_{\psi_w} = - \int_\Omega (Dw + Dw^\top) : Dh_{\psi_w} \, dx + \int_{\Gamma_\mathrm{d}} b \cdot h_{\psi_w} \, ds = 0, \tag{3.24}
$$

$$
\mathcal{L}_b h_b = - \int_{\Gamma_\mathrm{d}} h_b \cdot \psi_b + D_{\Gamma_\mathrm{d}} h_b : D_{\Gamma_\mathrm{d}} \psi_b \, ds + \int_{\Gamma_\mathrm{d}} h_b \cdot \psi_w \, ds = 0, \tag{3.25}
$$

$$
\mathcal{L}_{\psi_b} h_{\psi_b} = - \int_{\Gamma_\mathrm{d}} b \cdot h_{\psi_b} + D_{\Gamma_\mathrm{d}} b : D_{\Gamma_\mathrm{d}} h_{\psi_b} \, ds + \int_{\Gamma_\mathrm{d}} cn \cdot h_{\psi_b} \, ds = 0, \tag{3.26}
$$

$$
\mathcal{L}_c h_c = \alpha \int_{\Gamma_\mathrm{d}} c h_c \, ds + \int_{\Gamma_\mathrm{d}} h_c n \cdot \psi_b \, ds = 0, \tag{3.27}
$$

$$
\mathcal{L}_\lambda h_\lambda = \frac{h_\lambda}{d} \int_{\Gamma_\mathrm{d}} (x + w)^\top (D\tau)^{-\top} n J_\tau - x \cdot n \, ds = 0, \tag{3.28}
$$

$$
\mathcal{L}_\mu h_\mu = \sum_{i=1}^{d} (h_\mu)_i \int_{\Gamma_\mathrm{d}} (x_i + w_i)^2 \left((D\tau)^{-\top} n\right)_i J_\tau \, ds = 0 \tag{3.29}
$$

for all $(h_w, h_v, h_p, h_b, h_{\psi_w}, h_{\psi_v}, h_{\psi_p}, h_{\psi_b}, h_c, h_\lambda, h_\mu) \in W \times V \times \Pi \times B \times W_0 \times V_0 \times \Pi \times B \times L^2(\Gamma_\mathrm{d}) \times \mathbb{R} \times \mathbb{R}^d$. We thus obtain a system of nonlinear, coupled PDEs in a suitable form for standard finite element toolboxes.

3.5. On the semismoothness of the optimality system. We solve the system (3.20)–(3.29) with a semismooth Newton method. To justify this, we show semismoothness of the system and therefore take a closer look at the term in (3.20) that appears by differentiating

$$\frac{1}{2}\int_\Omega ((\eta_1 - J_\tau)_+)^2 dx = \int_\Omega (f_2 \circ \iota \circ f_1(w))(x)dx = F \circ \iota \circ f_1$$

with

$$\begin{aligned} f_1 &: H^s(\Omega)^d \to H^{s-1}(\Omega), \quad w \mapsto \eta_1 - J_\tau, \\ \iota &: H^{s-1}(\Omega) \to L^r(\Omega), \quad v \mapsto v, \\ f_2 &: L^r(\Omega) \to L^1(\Omega), \quad q \mapsto \frac{1}{2}(q)_+^2, \\ F &: L^r(\Omega) \to \mathbb{R}, \quad q \mapsto \int_\Omega \frac{1}{2}(q)_+^2 dx, \end{aligned}$$

$s > 1 + \frac{d}{2}$ and $2 \le r \le \infty$. Since $H^{s-1}(\Omega)$ is a Banach algebra for $s > 1 + \frac{d}{2}$, $f_1 : H^s(\Omega)^d \to H^{s-1}(\Omega)$ is $\mathcal{C}^\infty$. Since $s - 1 - \frac{d}{2} > 0$, the embedding ι is linear and continuous. The Nemytskii operator $f_2 : L^r(\Omega) \to L^1(\Omega)$ is Fréchet differentiable for $r \ge 2$ (see, e.g., [41, sect. 4.3.3]), and thus $F : q \mapsto \int_\Omega \frac{1}{2}(q)_+^2 dx$ is Fréchet differentiable as a mapping $L^r(\Omega) \to \mathbb{R}$ for $r \ge 2$ with derivative $F'(q) : L^r(\Omega) \to \mathbb{R}$, $h \mapsto \int_\Omega (q)_+ h dx$. Let $2 \le r < \infty$. Then $F' \in L^r(\Omega)^*$ as an element of the dual space of $L^r(\Omega)$ can be identified with $F'(q) = (q)_+ \in L^{r'}(\Omega)$, where $r' = \frac{r}{r-1}$. Now, by [44, Thm. 3.49], $q \mapsto (q)_+$ is locally Lipschitz and semismooth as a mapping $L^r(\Omega) \to L^{r'}(\Omega)$ for $r > 2$, which implies semismoothness of $w \mapsto F' \circ \iota \circ f_1$ as a mapping $H^s(\Omega)^d \to L^{r'}(\Omega)$ by [44, Prop. 3.8]. Hence, since $H^{s-1}(\Omega) \hookrightarrow L^\infty(\Omega)$ for $s > 1 + \frac{d}{2}$, the mapping $w \mapsto (F' \circ \iota \circ f_1) J_\tau (D\tau^{-1})_{i,k}$ is semismooth as an operator $H^s(\Omega)^d \to L^{r'}(\Omega)$ for all $i, k \in \{1, \dots, d\}$, and since $H^{s-1}(\Omega) \hookrightarrow L^r(\Omega)$ for $s > 1 + \frac{d}{2}$, the mapping

$$G : H^s(\Omega)^d \to (H^s(\Omega)^d)^*, \quad G(w)(h_w) := \int_\Omega (\eta_1 - J_\tau)_+ \operatorname{Tr}((D\tau)^{-1} D h_w) J_\tau \, dx \tag{3.30}$$

is semismooth.

3.6. Numerical results. In this section, we demonstrate the three proposed strategies S1–S3 in a 2d and a 3d case. In both cases, we consider a Stokes fluid in a flow tunnel with an obstacle in the center. Starting from a circular shape (in two dimensions) and a sphere (in three dimensions), the task is to optimize the shape such that the energy dissipation measured over the domain is minimized. This is a classical test case, which is investigated in detail, for instance, in [28].

The experimental settings in two dimensions are given by a rectangular domain $\Omega = [-10, 10] \times [-3, 3]$, where the initial obstacle is a circle with radius 0.5 and barycenter at $(0, 0)^\top$. We consider a flow along the x_1-axis which is modeled by the inflow velocity profile

$$v_{\text{in}} = \cos\left(\frac{2\|x\|_2 \, \pi}{\delta}\right), \tag{3.31}$$

where δ specifies the diameter of the inflow boundary in both two and three dimensions. This is consistent with the zero-velocity boundary conditions at the walls of

the flow tunnel. The particular choice of the inflow profile is made for comparability with the related works [34, 31] dealing with similar experiments.

The discretization of the domains is performed with the Delaunay method within the toolbox GMSH [13]. In two dimensions, we choose three different hierarchical grids with 1601, 6404, and 25 616 triangles. After each refinement, the grid at Γ_{d} is adapted to interpolate the circular obstacle and consists of 141, 282, and 564 line segments.

The 3d experiment is conducted in a cylindrical domain

$$\Omega \cup \Omega_{\mathrm{d}} = \left\{ x \in \mathbb{R}^3 : -10 \le x_1 \le 10, \sqrt{x_2^2 + x_3^2} \le 3 \right\},$$

where the initial obstacle is a sphere of radius 0.5 with barycenter $(0,0,0)^\top$. In this situation, Ω is discretized with 6994 surface triangles forming Γ_{d} and 118 438 tetrahedrons in the volume.

For all numerical computations in this section, we use the PDE toolbox-GETFEM++ [32]. We utilize the parallelized version of this library and provide the nonlinear optimality system (3.19)–(3.29) in the built-in language for weak formulations as it is. In order to solve the nonlinear system, second derivatives are computed symbolically by the library. While all terms but one in (3.19)–(3.29) are classically differentiable with respect to w, the integral in (3.19), which involves the nondifferentiable positive-part function $(\eta_1 - J_\tau)_+$, leads to a generalized derivative. Keeping in mind the discussion of the semismoothness of G in subsection 3.5, we obtain for the derivative of $-\gamma_1 G$

$$\begin{aligned}(3.32)\quad \gamma_1 \int_\Omega \chi_{(\eta_1 > J_\tau)} \operatorname{Tr}((D\tau)^{-1} D\bar{h}_w) \operatorname{Tr}((D\tau)^{-1} Dh_w) J_\tau^2 \\ + (\eta_1 - J_\tau)_+ \operatorname{Tr}((D\tau)^{-1} D\bar{h}_w (D\tau)^{-1} Dh_w) J_\tau \\ - (\eta_1 - J_\tau)_+ \operatorname{Tr}((D\tau)^{-1} Dh_w) \operatorname{Tr}((D\tau)^{-1} D\bar{h}_w) J_\tau \, dx\end{aligned}$$

for all $h_w, \bar{h}_w$. Corresponding to [43, eq. (4.1)], we can identify

$$-\chi_{(\eta_1 > J_\tau)} \operatorname{Tr}((D\tau)^{-1} D\bar{h}_w) J_\tau$$

in (3.32) with an element of the generalized differential of $(\eta_1 - J_\tau)_+$ evaluated in a direction $\bar{h}_w$.

For the discretization of the linearization matrix and the right-hand side in Newton's method, we choose piecewise linear basis functions for all variables except for the velocity v and its adjoint ψ_v. Here, we choose piecewise quadratic functions. A thorough justification for using nonconforming finite elements, e.g., with techniques in [4, sect. 8] and [5], is left for future research. For simplicity, in each iteration of Newton's method for the system (3.19)–(3.29), the parallel direct LU solver MUMPS [1] is applied.

Figure 3.1 depicts the 2d situation where color denotes the norm of the velocity field. The velocity profile in the 3d experiment is similar to the one shown in Figure 3.1 since we choose the domain Ω in three dimensions to be the rotation body of the 2d domain.

In all experiments in this section, $\epsilon_{\mathrm{ssn}} = 1 \times 10^{-9}$ is chosen as tolerance of the relative residual norm in the semismooth Newton method in Algorithm 3.2. Further, if the criterion is not fulfilled after $n_{\mathrm{ssn}} = 40$ steps, α is increased again.

In Figure 3.2, we compare the optimal solution for a regularization factor of $\alpha_{\mathrm{target}} = 10^{-10}$ for strategies S1–S3 on the finest grid with 25 616 triangles and 564

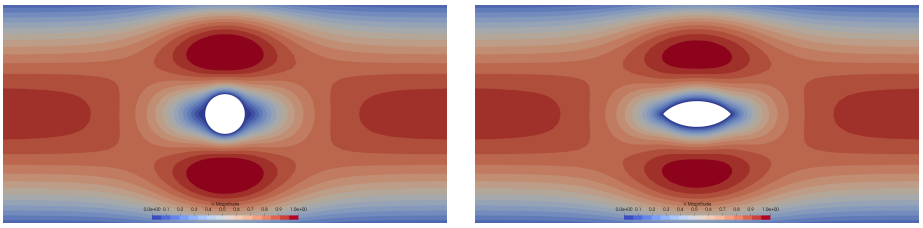

FIG. 3.1. *Holdall domain U and Stokes flow in $\Omega = U \setminus \Omega_{\mathrm{d}}$ on the left and the optimal, deformed configuration $\hat{\Omega}_{\mathrm{d}} = \tau(\Omega_{\mathrm{d}})$ on the right. Color denotes $\|v\|$ and $\|\hat{v}\|$, respectively.*

Algorithm 3.2 Optimization algorithm.

Require: $0 < \alpha_{\mathrm{target}} \leq \alpha_{\mathrm{init}}$, $0 < \alpha_{\mathrm{dec}} < 1$, $0 \leq \gamma_1$, $0 < \eta_1$, n_{ssn}, ϵ_{ssn}

Initialize all variables $(w, v, p, b, \psi_w, \psi_v, \psi_p, \psi_b, c, \lambda, \mu)_0$ with zero
$k \leftarrow 0$, $\alpha_k \leftarrow \alpha_{\mathrm{init}}$
while $\alpha_k \geq \alpha_{\mathrm{target}}$ **do**
  repeat
    Solve (3.20)–(3.29) for $(w, v, p, b, \psi_w, \psi_v, \psi_p, \psi_b, c, \lambda, \mu)_{k+1}$ with semismooth Newton method, $(w, v, p, b, \psi_w, \psi_v, \psi_p, \psi_b, c, \lambda, \mu)_k$ as initial guess and regularization parameter α_k
    if Newton's method did not converge to ϵ_{ssn} within n_{ssn} iterations **then**
      $\alpha_k \leftarrow \frac{1}{2}(\frac{\alpha_k}{\alpha_{\mathrm{dec}}} + \alpha_k)$
    end if
  until Newton's method converged
  $\alpha_{k+1} \leftarrow \alpha_{\mathrm{dec}} \alpha_k$
  $k \leftarrow k + 1$
end while

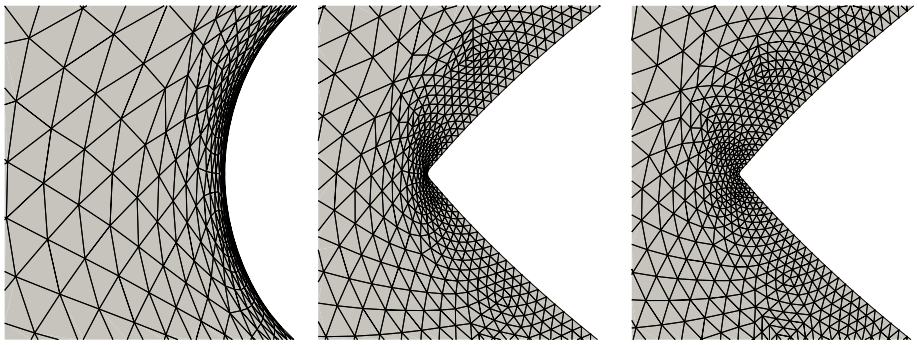

FIG. 3.2. *Optimal solution for regularization parameter $\alpha_{\mathrm{target}} = 10^{-10}$ following strategies* S1–S3 *(from left to right). The images show a 0.28×0.28 section centered at the point $(-0.8, 0.0)^\top$.*

surface elements. While in strategy S1 in the leftmost figure the optimal shape stays round at the tip, strategies S2 and S3 approximate the kink. This effect is further studied in the experiment shown in Figure 3.3. Here the optimal shapes according to a fixed parameter α_{target} are shown on a hierarchy of refined grid for strategies S1 (left) and S3 (right). The same holds true for the back of the shape, which is not shown here. For strategy S1, the condition $J_\tau = \det(I + Dw) \geq \eta_1 > 0$ becomes active. Figure 3.4 shows a zoom of the triangles with worst aspect ratio from the

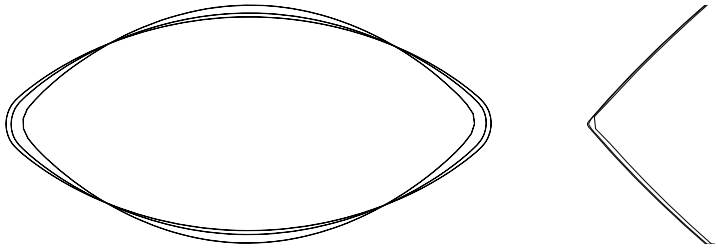

FIG. 3.3. *Optimal solution for regularization parameter* $\alpha_{\text{target}} = 10^{-10}$ *under grid refinements* $j = 1, 2, 3$, *i.e.* $1601 \cdot 4^{j-1}$ *triangles,* $141 \cdot 2^{j-1}$ *surface lines. Strategy* S1 *on the left-hand side and strategy* S3 *with a zoom on the nose of the shape.*

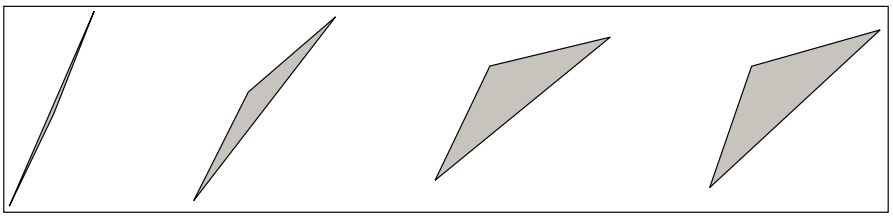

FIG. 3.4. *Triangles with worst aspect ratio in the experiment shown in Figure* 3.2 *for strategies* S1–S3 *and the mesh in the reference domain (from left to right).*

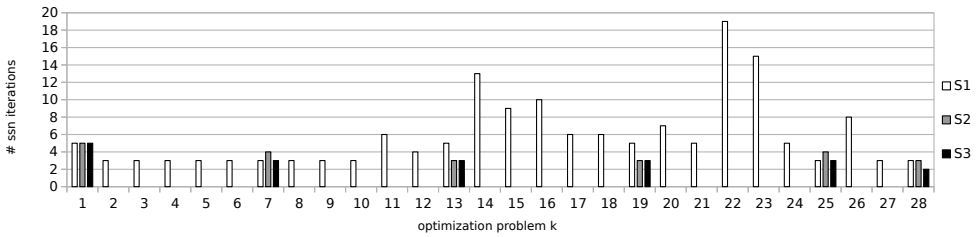

FIG. 3.5. *Semismooth Newton iteration counts with a tolerance of relative residual* $\epsilon_{\text{ssn}} = 1 \times 10^{-9}$ *for each subsequent optimization problem* k *with* $\alpha = 1 \times 10^{-2} \cdot \frac{1}{2}^{k-1}$, $\alpha_{\text{target}} = 1 \times 10^{-10}$. *For strategies* S2 *and* S3, $\alpha_{\text{dec}} = \frac{1}{64}$ *is chosen, thus intermediate problems are left out.*

experiment depicted in Figure 3.2 for strategies S1–S3. The rightmost triangle shows the worst from the undeformed domain as a reference. We observe that for $\eta_1 = 0.08$, it holds $J_\tau \in [\eta_1, 1.8]$ for strategy S1 while $J_\tau \in [0.085, 1.6]$ for strategies S2 and S3. Thus, the condition on J_τ is inactive in strategies S2 and S3. In this experiment, the parameter η_1 allows to control the worst-case degree of mesh degeneracy.

Numerical tests show that the choice of n_{ext} plays a decisive role for strategy S1. Since the reference shape Ω_{d} is either a circle in two dimensions or a sphere in three dimensions with barycenter zero, one can choose $n_{\text{ext}}(x) = \frac{x}{\|x\|_2}$ as an extension to the normal vector field on Γ_{d}. The numerical results for strategy S1 presented here are obtained for the choice $n_{\text{ext}}(x) = (\frac{1}{2} + \|x\|_2)^2 x$. Numerical experiments have shown that with the second choice of n_{ext}, we come closer to the optimal shapes resulting from strategies S2 and S3 than with the first variant. Parameter tuning might even lead to better results for strategy S1.

In Figure 3.5, the number of semismooth Newton iterations is depicted for each of the optimization problems. According to Algorithm 3.2, we utilize the optimal control

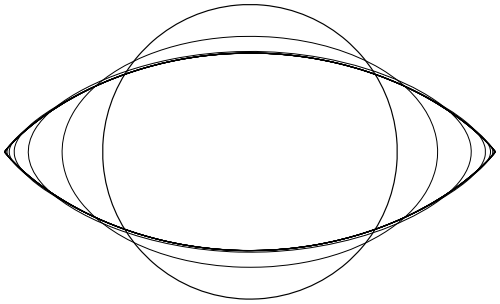

FIG. 3.6. *Optimal solution with regularization parameter* $\alpha = 10^{-k}$ *for* $k = 0, \ldots, 10$ *according to strategy* S3.

of one problem as initialization for the next one with smaller regularization parameter α. Computations are performed on the finest 2d grid considered in this section, i.e., $j = 3$. For all three strategies S1–S3, we choose $\alpha_{\text{init}} = 1 \times 10^{-2}$ and $\alpha_{\text{target}} = 1 \times 10^{-10}$. While for strategy S1 $\alpha_{\text{dec}} = \frac{1}{2}$ is required to guarantee convergence of the semismooth Newton method within $n_{\text{ssn}} = 40$, we proceed with $\alpha_{\text{dec}} = \frac{1}{64}$ for strategies S2 and S3. We observe that the number of required iterations significantly increases beginning in the 14th optimization problem for strategy S1. This can be explained by the positive part in the objective of (3.2) becoming nonzero, while for strategies S2 and S3, $J_\tau > \eta_1$ holds.

Furthermore, we investigate the convergence behavior of Algorithm 3.2 under hierarchical refinements. For example, strategy S3 on the three grids specified in the beginning of subsection 3.6 requires a total number of 22, 22, and 21 semismooth Newton iterations. Here we accumulate the iterations over all subsequent optimization problems with the corresponding regularization parameter α. The setup of $\epsilon, \alpha_{\text{init}}, \alpha_{\text{dec}}$, and α_{target} is the same as described for strategy S3 in the caption of Figure 3.5. These results suggest the expected mesh independent convergence of the semismooth Newton method.

In the next experiment, we consider strategies S1 and S3 under mesh refinements. Figure 3.3 shows the corresponding results for three hierarchically refined grids resulting in $1601 \cdot 4^{j-1}$ triangles and $141 \cdot 2^{j-1}$ surface lines for $j = 1, 2, 3$. The regularization parameter is again chosen as $\alpha_{\text{target}} = 10^{-10}$. The right-hand figure shows a zoom-in to the 0.28×0.28 square around the tip in order to make the shapes distinguishable. On the left-hand side, i.e., for strategy S1, we observe a slow grid convergence toward the theoretical, optimal shape. Strategy S3, in contrast, leads to comparable results even on relatively coarse grids.

Figure 3.6 visualizes the effect of the regularization parameter α. More precisely, a sequence of optimal shapes for different optimization problems depending on α are illustrated. The figure shows a transition for $\alpha = 10^{-k}$ for $k = 0, \ldots, 10$ according to strategy S3 on the finest grid; i.e., it presents the intermediate, optimal solutions one obtains after each iterations of Algorithm 3.2. It should be mentioned that this fine resolution in α is chosen for demonstration purposes only. For the specific example, we are able to choose an initial and decrement factor for α such that $\alpha_{\text{target}} = 10^{-10}$ is reached in two iterations of Algorithm 3.2. Since we are only interested in the optimal shape with respect to α_{target}, it is our intention to choose both α_{init} and α_{dec} in Algorithm 3.2 as small as possible. This choice is made heuristically depending on whether the semismooth Newton method in line Algorithm 3.2 converges within a prescribed number of iterations. If the inner iteration does not converge, we choose

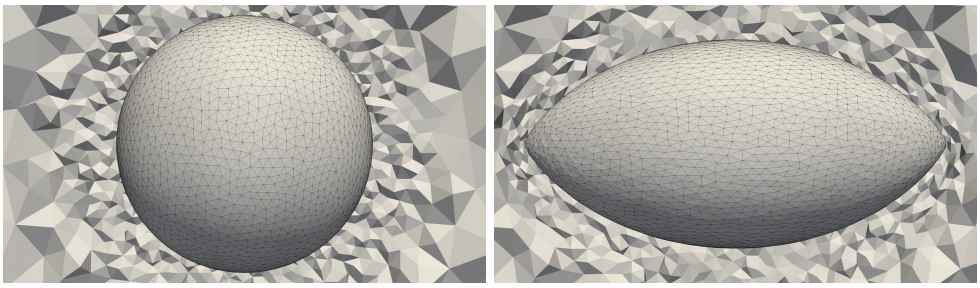

FIG. 3.7. *Reference* Ω_{d} *(left) and transformed shape* $\hat{\Omega}_{\mathrm{d}}$ *(right) according to optimal displacement* w *in 3d Stokes flow with a crinkled slice through the surrounding grid. The result is achieved with strategy* S3 *and* $\alpha_{\mathrm{target}} = 10^{-10}$.

α_{dec} closer to one. In all 2d computations, we choose the parameter $\eta_1 = 8 \times 10^{-2}$, $\gamma_1 = 1 \times 10^3$ independently of the α-strategy.

Figure 3.7 visualizes Algorithm 3.2 for 3d problems. It presents the reference shape Γ_{d} as the surface triangulation together with a slice through the tetrahedral grid of the reference domain Ω in the left subfigure. On the right-hand side, the effect of the optimal displacement field w to the shape $\hat{\Gamma}_{\mathrm{d}}$ and the volume $\hat{\Omega}$ is shown. As mentioned above, we are only interested in the optimal control c and the corresponding displacement field w for the regularization parameter α_{target}. In the 2d examples, this could be achieved with very few outer iterations of Algorithm 3.2, which means that one could start with a small α_{init} and proceed fast toward α_{target}. However, in the 3d case, it turns out that a more careful strategy has to be considered in order to obtain convergence of Newton's method within n_{ssn} steps. The results shown in Figure 3.7 are obtained with $\alpha_{\mathrm{init}} = 1 \times 10^{-1}$, $\alpha_{\mathrm{target}} = 1 \times 10^{-6}$, $\alpha_{\mathrm{dec}} = 0.5$, $\eta_1 = 8 \times 10^{-2}$, and $\gamma_1 = 1 \times 10^3$.

4. Conclusion and outlook. We presented a formulation of shape optimization problems based on the method of mappings that is motivated from a continuous perspective. Using this approach replaced the problem of preventing mesh degeneration by the question of finding a suitable set of admissible transformations. It was demonstrated how the quality of the reference discretization can be maintained by suitable choices of extension operators. We proposed a method such that the set of admissible transformations is a subset of the space of $\mathcal{C}^1$-diffeomorphisms. Numerical simulations substantiated the versatility of this approach and indicated mesh independence. For the sake of convenience, we worked with a closed and smooth shape boundary. The assumptions can be alleviated by thorough choices of the operator S. Furthermore, our approach allows for refinement and relocation strategies during the optimization process and can also be combined with adaptive mesh refinement strategies and globalized trust region methods. This, however, is left for future research.

REFERENCES

[1] P. R. AMESTOY, A. GUERMOUCHE, J.-Y. L'EXCELLENT, AND S. PRALET, *Hybrid scheduling for the parallel solution of linear systems*, Parallel Comput., 32 (2006), pp. 136–156.

[2] S. BASTING, A. QUAINI, S. ČANIĆ, AND R. GLOWINSKI, *Extended ALE method for fluid–structure interaction problems with large structural displacements*, J. Comput. Phys., 331 (2017), pp. 312–336.

[3] C. BRANDENBURG, F. LINDEMANN, M. ULBRICH, AND S. ULBRICH, *A continuous adjoint approach to shape optimization for Navier Stokes flow*, in Optimal Control of Coupled

Systems of Partial Differential Equations, K. Kunisch, G. Leugering, J. Sprekels, and F. Tröltzsch, eds., Internat. Ser. Numer. Math. 160, Birkhäuser, Basel, 2009, pp. 35–56.
[4] S. C. Brenner and L. R. Scott, *The Mathematical Theory of Finite Element Methods*, Springer, New York, 2008, https://doi.org/10.1007/978-0-387-75934-0.
[5] F. Brezzi and M. Fortin, eds., *Mixed and Hybrid Finite Element Methods*, Springer, New York, 1991, https://doi.org/10.1007/978-1-4612-3172-1.
[6] A. Brudnyi and Y. Brudnyi, *Methods of Geometric Analysis in Extension and Trace Problems.* Vol. 102, Birkhäuser, Basel, 2012.
[7] J. S. Dokken, S. K. Mitusch, and S. W. Funke, *Automatic Shape Derivatives for Transient PDEs in FEniCS and Firedrake*, preprint, https://arxiv.org/abs/2001.10058, 2020.
[8] C. Elliott and H. Fritz, *On algorithms with good mesh properties for problems with moving boundaries based on the harmonic map heat flow and the DeTurck trick*, SIAM J. Comput. Math., 2 (2016), pp. 141–176.
[9] T. Etling, R. Herzog, E. Loayza, and G. Wachsmuth, *First and second order shape optimization based on restricted mesh deformations*, SIAM J. Sci. Comput., 42 (2020), pp. A1200–A1225, https://doi.org/10.1137/19M1241465.
[10] M. Fischer, F. Lindemann, M. Ulbrich, and S. Ulbrich, *Fréchet differentiability of unsteady incompressible Navier-Stokes flow with respect to domain variations of low regularity by using a general analytical framework*, SIAM J. Control Optim., 55 (2017), pp. 3226–3257, https://doi.org/10.1137/16M1089563.
[11] P. Gangl, A. Laurain, H. Meftahi, and K. Sturm, *Shape optimization of an electric motor subject to nonlinear magnetostatics*, SIAM J. Sci. Comput., 37 (2015), pp. B1002–B1025.
[12] H. Garcke, M. Hinze, and C. Kahle, *A stable and linear time discretization for a thermodynamically consistent model for two-phase incompressible flow*, Appl. Numer. Math., 99 (2016), pp. 151–171.
[13] C. Geuzaine and J.-F. Remacle, *Gmsh: A 3-D finite element mesh generator with built-in pre- and post-processing facilities*, Internat. J. Numer. Methods Engrg., 79 (2009), pp. 1309–1331, https://doi.org/10.1002/nme.2579.
[14] H. Harbrecht and J. Tausch, *On the numerical solution of a shape optimization problem for the heat equation*, SIAM J. Sci. Comput., 35 (2013), pp. A104–A121.
[15] J. Haubner, *Shape Optimization for Fluid-Structure Interaction*, dissertation, Technische Universität München, München, 2020.
[16] J. Haubner, M. Ulbrich, and S. Ulbrich, *Analysis of shape optimization problems for unsteady fluid-structure interaction*, Inverse Problems, 36 (2020), 034001, https://doi.org/10.1088/1361-6420/ab5a11.
[17] M. Hintermüller and W. Ring, *A second order shape optimization approach for image segmentation*, SIAM J. Appl. Math., 64 (2004), pp. 442–467.
[18] R. Hiptmair, L. Scarabosio, C. Schillings, and C. Schwab, *Large deformation shape uncertainty quantification in acoustic scattering*, Adv. Comput. Math., 44 (2018), pp. 1475–1518, https://doi.org/10.1007/s10444-018-9594-8.
[19] S. Hofmann, M. Mitrea, and M. Taylor, *Geometric and transformational properties of Lipschitz domains, Semmes-Kenig-Toro domains, and other classes of finite perimeter domains*, J. Geom. Anal., 17 (2007), pp. 593–647, https://doi.org/10.1007/BF02937431.
[20] J. A. Iglesias, K. Sturm, and F. Wechsung, *Two-dimensional shape optimization with nearly conformal transformations*, SIAM J. Sci. Comput., 40 (2018), pp. A3807–A3830.
[21] G. Katriel, *Mountain pass theorems and global homeomorphism theorems*, in Annales de l'Institut Henri Poincare (C) Non Linear Analysis, Vol. 11, Elsevier, Amsterdam, 1994, pp. 189–209.
[22] M. Keuthen and M. Ulbrich, *Moreau-Yosida regularization in shape optimization with geometric constraints*, Comput. Optim. Appl., 62 (2015), pp. 181–216, https://doi.org/10.1007/s10589-014-9661-0.
[23] B. Khoromskij and G. Wittum, *Elliptic Poincaré-Steklov Operators*, Springer, New York, 2004, pp. 37–62, https://doi.org/10.1007/978-3-642-18777-3_2.
[24] B. Kiniger and B. Vexler, *A priori error estimates for finite element discretizations of a shape optimization problem*, ESAIM Math. Model. Numer. Anal., 47 (2013), pp. 1733–1763, https://doi.org/10.1051/m2an/2013086.
[25] K. Kunisch and G. Peichl, *Numerical gradients for shape optimization based on embedding domain techniques*, Comput. Optim. Appl., 18 (2001), pp. 95–114.
[26] G. Lieberman, *Mixed boundary value problems for elliptic and parabolic differential equations of second order*, J. Math. Anal. Appl., 113 (1986), pp. 422–440.
[27] J.-L. Lions and E. Magenes, *Non-Homogeneous Boundary Value Problems and Applications.* Vol. 1, Springer, New York, 1972.

[28] B. Mohammadi and O. Pironneau, *Applied Shape Optimization for Fluids*, Oxford University Press, Oxford, 2010.
[29] F. Murat and J. Simon, *Etude de problèmes d'optimal design*, in Optimization Techniques Modeling and Optimization in the Service of Man Part 2: Proceedings, 7th IFIP Conference Nice, September 8–12, 1975, J. Cea, ed., Springer, New York, 1976, pp. 54–62.
[30] A. Nägel, V. Schulz, M. Siebenborn, and G. Wittum, *Scalable shape optimization methods for structured inverse modeling in 3D diffusive processes*, Comput. Vis. Sci., 17 (2015), pp. 79–88, https://doi.org/10.1007/s00791-015-0248-9.
[31] S. Onyshkevych and M. Siebenborn, *Mesh Quality Preserving Shape Optimization Using Nonlinear Extension Operators*, https://arxiv.org/abs/2006.04420, 2020.
[32] Y. Renard and J. Pommier, *GetFEM++ Finite Element Library*, http://www.getfem.org, 2018.
[33] S. Schmidt, C. Ilic, V. Schulz, and N. R. Gauger, *Three-dimensional large-scale aerodynamic shape optimization based on shape calculus*, AIAA J., 51 (2013), pp. 2615–2627.
[34] V. Schulz and M. Siebenborn, *Computational comparison of surface metrics for PDE constrained shape optimization*, Comput. Methods Appl. Math., 16 (2016), pp. 485–496, https://doi.org/10.1515/cmam-2016-0009.
[35] V. Schulz, M. Siebenborn, and K. Welker, *Structured inverse modeling in parabolic diffusion problems*, SIAM J. Control Optim., 53 (2015), pp. 3319–3338, https://doi.org/10.1137/140985883.
[36] V. Schulz, M. Siebenborn, and K. Welker, *Efficient PDE constrained shape optimization based on Steklov–Poincaré-type metrics*, SIAM J. Optim., 26 (2016), pp. 2800–2819, https://doi.org/10.1137/15M1029369.
[37] M. Siebenborn and K. Welker, *Algorithmic aspects of multigrid methods for optimization in shape spaces*, SIAM J. Sci. Comput., 39 (2017), pp. B1156–B1177.
[38] T. Slawig, *Shape optimization for semi-linear elliptic equations based on an embedding domain method*, Appl. Math. Optim., 49 (2004), pp. 183–199, https://doi.org/10.1007/s00245-003-0787-1.
[39] J. Sokolowski and J.-P. Zolesio, *Introduction to Shape Optimization: Shape Sensitivity Analysis*, Vol. 16, Springer, New York, 2012.
[40] M. Taylor, *Partial Differential Equations* I: *Basic Theory,* 2*nd ed.*, Springer, New York, 2011.
[41] F. Tröltzsch, *Optimal Control of Partial Differential Equations. Theory, Methods and Applications*, Vol. 112, American Mathematical Society, Providence, RI, 2010.
[42] R. Udawalpola and M. Berggren, *Optimization of an acoustic horn with respect to efficiency and directivity*, Internat. J. Numer. Methods Engrg., 73 (2008), pp. 1571–1606.
[43] M. Ulbrich, *Semismooth Newton methods for operator equations in function spaces*, SIAM J. Optim., 13 (2002), pp. 805–841, https://doi.org/10.1137/s1052623400371569.
[44] M. Ulbrich, *Semismooth Newton Methods for Variational Inequalities and Constrained Optimization Problems in Function Spaces*, SIAM, Philadelphia, 2011, https://doi.org/10.1137/1.9781611970692.
[45] D. N. Wilke, S. Kok, and A. A. Groenwold, *A quadratically convergent unstructured remeshing strategy for shape optimization*, Internat. J. Numer. Methods Engrg., 65 (2005), pp. 1–17, https://doi.org/10.1002/nme.1430.